Supporting Information for:

Polymer-iron oxide nanofiber composites for lead removal:
Performance improvements through organic acid stabilization of nanoparticles to promote surface segregation during electrospinning

Sewoon Kim[1], Yun Young Choi[2], Chang Min Park[3], Nosang V. Myung[2], David M. Cwiertny[1,4]*

[1]Department of Civil and Environmental Engineering, University of Iowa, 4105 Seamans Center, Iowa City, IA 52242, USA

[2]Department of Chemical and Biomolecular Engineering, University of Notre Dame, IN 26556, USA

[3]Department of Civil and Environmental Engineering, Kyungpook National University, Daegu 41566, Republic of Korea

[4]Department of Chemistry, University of Iowa, E331 Chemistry Building 230 North Madison Street, Iowa City, IA 52242

*Corresponding author:
E-mail: david-cwiertny@uiowa.edu (D.M. Cwiertny)

Prepared for *Environmental Science: Nano*

7 Tables, 19 Figures, and 34 Pages

*Corresponding author contact information:
Phone: +1-319-335-1401; Fax: +1-319-335-5660;
Email: david-cwiertny@uiowa.edu;
Mail: Department of Civil and Environmental Engineering
4105 Seamans Center, Iowa City, IA 52242

I. Supplemental Materials and Methods

Chemicals. Iron oxide particles were obtained from 7 different vendors. The properties of iron oxide are described in Table 1 of the main text. Polyacrylonitrile (PAN; MW 150,000) and N,N-dimethylformamide (DMF; 99.8%) were used in the electrospinning of all nanofibers as the polymer and solvent, respectively. Sodium dodecyl sulfate (SDS; $\geq$ 99.9%), ortho-phthalic acid (PTA; $\geq$ 99.5%), tera-phthalic acid (TPA; 98%) and ethylenediaminetetraacetic acid (EDTA; $\geq$99%)) were used as organic acid additives (OAs). Lead (Pb) stock solution was prepared by using lead nitrate (Pb(NO$_3$)$_2$; > 99%). For sorption studies, 10 mM HEPES buffer ($\geq$ 99%) was used, and solution pH was adjusted to the desired value with 5 N NaOH. For Pb analysis, samples were acidified by nitric acid (HNO$_3$; 70%). All chemicals except for iron oxide particles were obtained from Sigma-Aldrich (St. Louis, MO, USA) and used as received.

Electrospinning conditions. The prepared sol gels were loaded into a 12 mL plastic syringe. After placing the syringe onto a syringe pump, the syringe was connected to a female luer lock fitting, polyethylene tubing, metal nozzle adapter, male luer lock fitting, and needle, in that order. The needle tip was located 10 cm from a rotating metal drum collector. To collect nanofibers, the metal drum was covered in Al Foil. A pumping rate of 0.5 mL/h was used for the syringe pump, and a rotating speed of 550 rpm was used for the drum collector. During electrospinning, 15 kV of voltage was applied to the needle tip. Conditions inside the electrospinning chamber were 20% relative humidity and a temperature of 20 °C. Upon completion, the nanofiber mat was peeled off from Al foil and subsequently used in sorption studies.

Materials characterization. An X-ray diffractometer (XRD) with a cobalt X-ray source (MiniFlex II, Rigaku) was used to confirm the mineral phase of all commercially available iron

oxide particles across values of 2θ from 10° to 80° at an interval of 0.02°. To measure zeta potential values of iron oxide particle suspensions, we used a zeta-potential analyzer (Zetasizer Nano-ZS, Malvern). Scanning electron microscopy (SEM; S4800, Hitachi) was used to investigate the morphology of electrospun nanofiber mats at an acceleration voltage of 1.5 kV. Before SEM analysis, all samples were sputter-coated with a thin layer of gold. The measured SEM images were used to evaluate fiber diameters from measurement of > 150 nanofibers in ImageJ software. The morphology of iron oxide particles and nanofiber composites also was examined using transmission electron microscopy (TEM; HT7800, Hitachi). Samples for TEM imaging were prepared via sonication of a dilute suspension in DI water, from which a droplet was withdrawn and allowed to dry on a TEM grid prior to imaging. N_2-BET analysis (NOVA 4200e, Quantachrome) was used to estimate surface area and pore volume for the nanofiber mats. The samples were degassed at 35°C for 12h. Fourier Transform Infrared Spectroscopy (FTIR; Frontier, PerkinElmer) was performed to investigate the functional groups on the electrospun nanofiber mats. Lastly, XPS (NEXSA, ThermoFisher) with Al Kα X-ray source was applied to confirm the elemental distributions. XPS was used to collect full spectrum survey scans, as well as to examine the Fe2p region.

Sorption data modeling. The adsorption capacity and removal efficiency of the iron oxide particles and nanofiber mats were calculated at equilibrium using Eqs. S1 and S2:

$$\text{Adsorption capacity (mg/g)} = \frac{\frac{C_i - C_e}{m} \cdot V}{} \qquad \text{(S1)}$$

$$\text{Removal efficiency (\%)} = \frac{\left(\frac{C_i - C_e}{C_i}\right) \times 100}{} \qquad \text{(S2)}$$

where C_i and C_e are the initial and equilibrium concentrations of Pb in solution (mg/L), respectively; and V is the solution volume (L); m is the sorbent mass (mg). Sorption isotherms were described

using both Langmuir and Freundlich isotherm models as represented in Eqs. S3 and S4, respectively.

$$\text{Langmuir:} \quad q_e = \frac{q_m K_L C_e}{1 + K_L C_e} \tag{S3}$$

$$\text{Freundlich:} \quad q_e = K_F C_e^{\frac{1}{n_F}} \tag{S4}$$

where q_e is the sorbed Pb concentration at equilibrium (mg/g); q_m is the maximum Pb sorption capacity at monolayer surface (mg/g); C_e is the concentration of Pb in the aqueous phase at equilibrium (mg/L); K_L is the Langmuir sorption coefficient (L/mg); K_F is the Freundlich sorption coefficient; and $\frac{1}{n_F}$ is the heterogenicity factor associated with the intensity of sorption.

II. Supplemental Results and Discussion

Pb sorption on different commercially available Fe particles

Fig. S3(a) shows the extent of Pb sorption (10 mg/L of initial, total dissolved Pb) over time in particle suspensions (0.2 g/L) of each of the seven commercially available Fe oxides (Vendors A through G) evaluated for composite nanofiber synthesis. At this initial dissolved Pb concentration, the greatest extent of sorption was approximately ~40 mg/g for the Fe oxide from vendor C, with the lowest capacity observed for vendor G at ~10 mg/g. All Fe oxides exhibited similar time dependent profiles in Pb sorption, with rapid uptake within the first 2 h and little (typically < 10% of the observed total for Pb sorption) additional Pb sorption thereafter. The initially fast and then slower regimes of Pb sorption follows expectations from prior studies; Pb is first rapidly taken up on the external binding sites on the oxide surface, after which sorption occurs more slowly under possible diffusion limitations at internal sites within particles and particle aggregates.

Corresponding Pb isotherms for Fe oxide particle suspensions are shown in Fig. S3b, and key parameters from isotherm model fitting are summarized in Table S2. Based on the observed relationship between sorbed Pb and dissolved Pb at equilibrium, sorption was best described by the Langmuir isotherm model, and these model fits (obtained by non-linear regression) are also provided in Fig. S3b. This was most evident for those Fe oxides with lower Pb sorption capacity, where clear evidence of surface saturation was observed in Pb isotherm experiments. Because Langmuir model fits were generally stronger (based on correlation coefficient (R^2)) than those obtained using a Freundlich model, we assessed sorption capacity for all materials based on the maximum sorbed Pb concentration (q_{max} values) estimated from the Langmuir model. As with the Pb uptake rate studies, the largest q_{max} value was observed for the Fe oxide from vendor C (~120

mg/g $\pm$ 0.7), whereas the lowest q_{max} value was obtained for the material from vendor G (~25 mg/g $\pm$ 0.6).

Key properties of the commercial Fe oxides studied herein, including their vendor-reported particle size, specific surface area and total pore volume from N_2-BET analysis, and cost (per g) are summarized in Table 1 of the main text. Vendor-reported primary article sizes ranged from 3 nm to 50 μm, and generally surface area (from ~5 to 160 m^2/g), pore volume (~0.02 to 1.6 cm^3/g), and cost (~0.001 to 1.8 USD/g) increased with decreasing particle size. From XRD analysis (Fig. S4), diffraction patterns for Fe oxide from vendors A, B, C, and G were consistent with reference diffraction pattern (PDF 98-000-0060; JADE Software) for hematite, whereas maghemite was identified as the primary phase for powders from vendors D and F (PDF 98-000-1056; JADE software). For the material from vendor E, hematite appeared to be the dominant crystal phase, but a yet unidentified secondary phase was also present (see Fig. S4). TEM images (Fig. S5) revealed that particles were roughly spherical in shape and comparable in size to the values provided by the vendor.

From particle properties in Table 1 of the main text, trends in Pb sorption capacity generally can be explained by differences in the iron oxide particle size and corresponding specific surface area, as well as iron oxide surface charge. Smaller particles with higher specific surface area result in higher Pb sorption capacity, as is expected from established trends in the size-dependent performance of sorbent particles.[S1,S2] Zeta potential data (Fig. S6) were also mostly consistent with the observed trends in Pb sorption capacity. Negatively charged Fe oxides at pH 6.5 typically exhibited higher Pb sorption capacity, although particle size and surface area were still important factors. For example, the Fe oxide from vendor E exhibited the second lowest (*i.e.,* most negative) zeta potential at pH 6.5, but still resulted in relatively low Pb sorption capacity because of its bigger

particle size (*i.e.,* lower specific surface area). Fig. S7a shows the relationship between Pb uptake capacity (based on q_{max} values from Langmuir isotherm modeling of experimental sorption data in Fig. S3b) and vendor-reported particle size for all commercial Fe oxides investigated herein. Indeed, there is a nearly linear decrease in q_{max} values with increasing particle size (on a logarithmic scale) across all materials, regardless of whether the Fe oxide mineralogy is primarily hematite or maghemite.

Table S1. Water quality for particulate lead filtration experiments.

Parameters	NSF/ANSI 53	This study
pH	8.30 ~ 8.60	8.5 ± 0.2
Total lead (mg/L)	$150.0 \pm 10\%$	161.6
Total Particulate lead % (>0.1 μm)	$30.0 \pm 10\%$	29.1%

Table S2. Langmuir and Freundlich isotherm model parameters for seven different commercially available Fe oxide particles used in Pb sorption isotherm experiments (see Fig. S3b). Values were determined through least squares non-linear regression analysis using Microsoft Excel.

Material	Langmuir			Freundlich		
	q_{max}	K_L	R^2	n	K_F	R^2
A	87.1 ± 0.9	0.9 ± 0.1	0.9984	1.5 ± 0.1	35.1 ± 1.9	0.9693
B	73.6 ± 0.8	0.4 ± 0.1	0.9994	1.4 ± 0.2	19.3 ± 2.3	0.9931
C	120 ± 0.7	1.1 ± 0.2	0.9999	1.3 ± 0.1	64.3 ± 2.9	0.9918
D	83.8 ± 0.5	1.2 ± 0.5	0.9996	1.6 ± 0.3	33.1 ± 1.5	0.9745
E	40.8 ± 0.7	0.3 ± 0.1	0.9995	1.5 ± 0.4	9.1 ± 0.8	0.9907
F	49.7 ± 0.7	1.0 ± 0.3	0.999	1.9 ± 0.5	17.2 ± 1.2	0.9706
G	25.6 ± 0.6	0.2 ± 0.1	0.9986	1.5 ± 0.2	3.5 ± 0.7	0.9960

Table S3. Langmuir and Freundlich isotherm model parameters for Fe oxide-containing PAN composites (Fe-PAN) prepared with Fe oxides from Vendors B, D, and E across a range of different Fe oxide loadings (from 1 to 8 wt.% relative to total sol-gel mass). Isotherm data and model fits are shown in Fig. S14. All composites were prepared without organic additives.

Material		Langmuir			Freundlich		
		q_{max}	K_L	R^2	n	K_F	R^2
B	Fe1	7.0 ± 0.3	0.5 ± 0.1	0.9984	2.4 ± 0.2	2.0 ± 0.1	0.9186
	Fe2	9.4 ± 0.5	0.4 ± 0.2	0.9978	2.1 ± 0.1	2.3 ± 0.3	0.9223
	Fe3	10.2 ± 1.3	2.6 ± 0.5	0.9917	3.0 ± 0.2	4.6 ± 0.2	0.9561
	Fe4	12.7 ± 0.2	0.7 ± 0.5	0.9989	2.3 ± 0.3	4.0 ± 0.2	0.9126
	Fe5	11.7 ± 0.7	5.2 ± 0.4	0.9926	3.2 ± 0.2	6.0 ± 1.5	0.9660
	Fe8	12.0 ± 0.6	5.8 ± 0.3	0.9892	3.1 ± 1.0	6.2 ± 2.0	0.9650
D	Fe1	9.0 ± 0.2	1.1 ± 0.3	0.9938	2.7 ± 0.1	3.4 ± 1.5	0.9579
	Fe2	9.4 ± 0.7	3.3 ± 1.3	0.9841	3.0 ± 0.3	4.5 ± 0.2	0.9810
	Fe3	11.9 ± 1.3	2.9 ± 0.7	0.9839	2.7 ± 0.4	5.4 ± 2.1	0.9844
	Fe4	12.5 ± 4.3	1.8 ± 0.6	0.9915	2.4 ± 0.4	5.3 ± 0.7	0.9715
	Fe5	15.6 ± 1.1	3.4 ± 0.5	0.9955	2.8 ± 0.6	7.6 ± 0.7	0.9282
	Fe8	17.5 ± 2.3	1.4 ± 0.5	0.9983	2.4 ± 1.1	6.7 ± 0.3	0.9132
E	Fe1	7.8 ± 0.8	0.5 ± 0.5	0.9889	2.1 ± 2.3	2.0 ± 0.4	0.9842
	Fe2	9.7 ± 2.0	0.4 ± 0.2	0.9989	2.1 ± 0.6	2.3 ± 1.4	0.9489
	Fe3	9.3 ± 0.6	0.9 ± 0.2	0.9822	2.3 ± 0.9	3.1 ± 0.2	0.9698
	Fe4	10.5 ± 0.8	1.6 ± 0.9	0.9985	2.2 ± 1.2	3.2 ± 0.9	0.9137
	Fe5	12.0 ± 0.5	0.5 ± 0.6	0.9896	2.7 ± 0.4	4.3 ± 0.7	0.9567
	Fe8	15.5 ± 0.4	0.3 ± 1.1	0.9952	2.1 ± 0.5	3.5 ± 2.3	0.9132
PAN		1.4 ± 1.1	1.9 ± 0.3	0.5568	4.0 ± 0.5	0.8 ± 0.1	0.8204

Table S4. Performance and cost analysis of Fe-PAN nanofiber composites. The performance (mg/Pb/g mat) represents q_{max} values from isotherms in Fig. S14 and summarized in Table S3. The cost was calculated as the sum of all raw materials used in nanofiber fabrication including PAN, DMF, and Fe. The removed Pb (in mg/$) was evaluated by multiplying the performance by composite synthesis cost.

Material		Performance (mg Pb/g mat)	Cost for synthesis (g/$)	Removed Pb (mg/$)
B	Fe1	7.0 ± 0.3	0.2	1.4
	Fe2	9.4 ± 0.5	0.3	2.8
	Fe3	10.2 ± 1.3	0.3	3.1
	Fe4	12.7 ± 0.2	0.3	3.8
	Fe5	11.7 ± 0.7	0.3	3.5
	Fe8	12.0 ± 0.6	0.3	3.6
D	Fe1	9.0 ± 0.2	0.1	0.9
	Fe2	9.4 ± 0.7	0.2	1.9
	Fe3	11.9 ± 1.3	0.2	2.4
	Fe4	12.5 ± 4.3	0.2	2.5
	Fe5	15.6 ± 1.1	0.2	3.1
	Fe8	17.5 ± 2.3	0.2	3.5
E	Fe1	7.8 ± 0.8	0.1	0.8
	Fe2	9.7 ± 2.0	0.2	1.9
	Fe3	9.3 ± 0.6	0.2	1.9
	Fe4	10.5 ± 0.8	0.2	2.1
	Fe5	12.0 ± 0.5	0.2	2.4
	Fe8	15.5 ± 0.4	0.3	4.7
PAN		1.4 ± 1.1	0.2	0.3

Table S5. Langmuir and Freundlich isotherm model parameters of unrinsed (top) and rinsed (bottom) Fe-PAN nanofiber composites containing different organic additives.

Material		Langmuir	
		q_{max}	K_L
Unrinsed	Fe5-SDS1	21.3 ± 0.2	2.1 ± 0.9
	Fe5-SDS2	23.4 ± 0.2	6.5 ± 0.6
	Fe5-SDS3	33.1 ± 0.7	7.0 ± 0.3
	Fe5-SDS4	34.0 ± 0.3	9.0 ± 1.2
	Fe5-SDS3+PTA1	36.0 ± 0.3	19.4 ± 0.3
	Fe5-SDS3+PTA2	36.3 ± 0.2	23.3 ± 0.8
	Fe5-SDS3+PTA3	40.0 ± 0.1	20.0 ± 2.2
	Fe5-PTA3	39.0 ± 0.6	18.6 ± 1.2
	Fe5-PTA5	44.8 ± 0.2	20.9 ± 0.7
Rinsed	Fe5-SDS1	17.0 ± 0.1	1.0 ± 0.6
	Fe5-SDS2	19.0 ± 0.3	4.0 ± 1.1
	Fe5-SDS3	24.6 ± 0.2	3.7 ± 1.3
	Fe5-SDS4	26.4 ± 0.1	4.9 ± 0.9
	Fe5-SDS3+PTA1	30.2 ± 0.8	15.1 ± 4.1
	Fe5-SDS3+PTA2	34.7 ± 0.4	13.0 ± 5.2
	Fe5-SDS3+PTA3	38.0 ± 0.1	15.4 ± 1.4
	Fe5-PTA3	38.0 ± 0.2	16.0 ± 0.9
	Fe5-PTA5	40.1 ± 0.5	16.2 ± 1.2

Table S6. Surface-area-normalized Pb uptake based on maximum adsorption capacities from Langmuir model at pH 6.5. For comparison,

Material	mg Pb / m^2 material
PAN	0.1
Fe5(B)	0.8
Fe5(B)-SDS3	2.8
Fe5(B)-SDS(R)	0.6
Fe5(B)-PTA3	4.5
Fe5(B)-PTA(R)	1.5
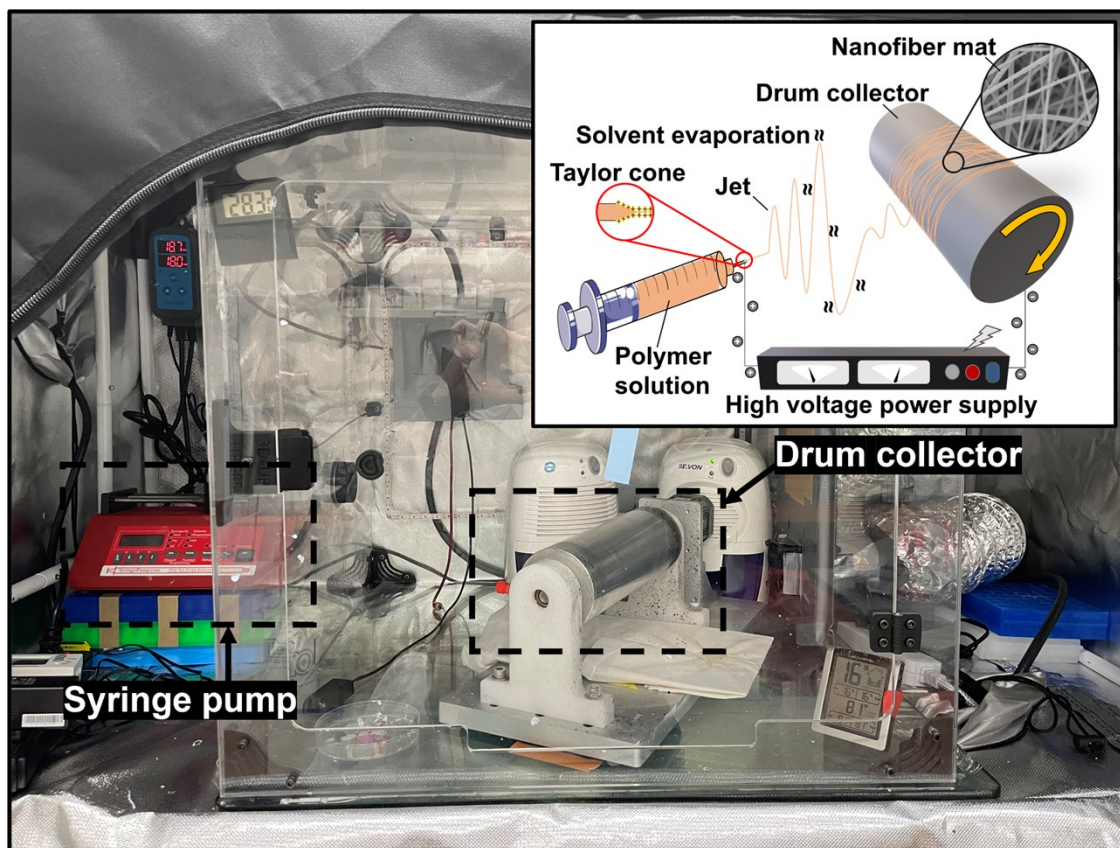
Fig. S1. Electrospinning rig with schematic of nanofiber fabrication via electrospinning (inset), in which a polymer sol gel solution emitted from a syringe pump, under the forces from surface tension and an applied electric field, produces a Taylor cone that results in a fine jet of fibers that is deposited on a grounded rotating drum collector.
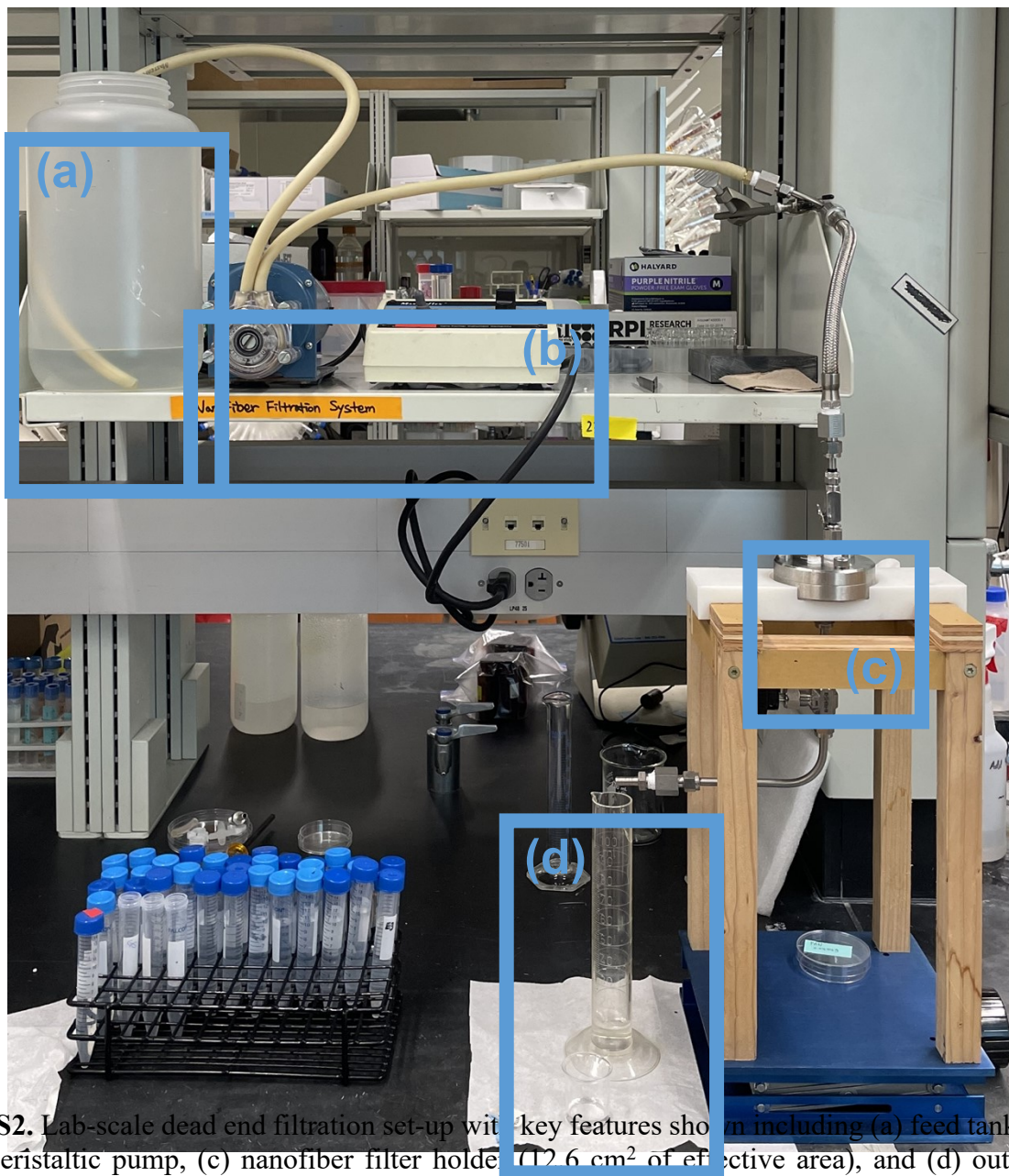
Fig. S2. Lab-scale dead end filtration set-up with key features shown including (a) feed tank (4L), (b) peristaltic pump, (c) nanofiber filter holder (12.6 cm^2 of effective area), and (d) outlet for sample collection.
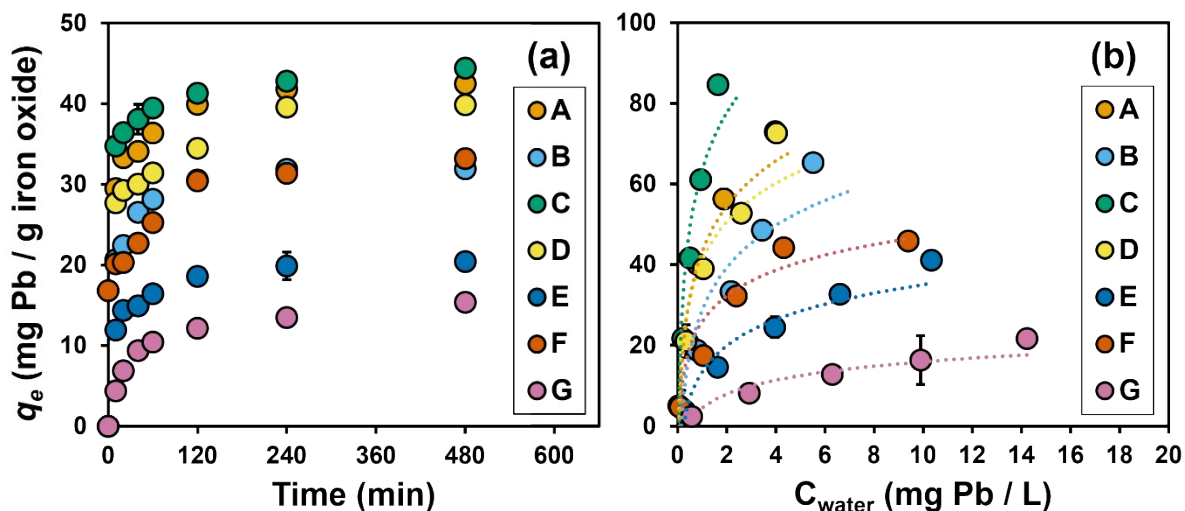
Fig. S3. Pb uptake performance comparison of seven different commercial Fe oxide particles based on (a) rates of Pb uptake and (b) sorption isotherms. The dashed lines in (b) represent Langmuir isotherm model best fits obtained by non-linear regression analysis, results of which are summarized in Table S2. All data represent the average (with standard deviation) from replicate experiments. Experimental conditions: (a) Initial Pb concentration ($C_{initial}$) = 10 mg/L as Pb; pH = 6.5 with 10 mM HEPES buffer; T = 20 ^{o}C; dosage = 0.2 g/L; contact time = 0-24 h (b) $C_{initial}$ = 1-40 mg/L as Pb; pH=6.5 with 10 mM HEPES buffer; T = 20°C; dosage = 0.2 g/L; time to equilibrium = 24 hr.
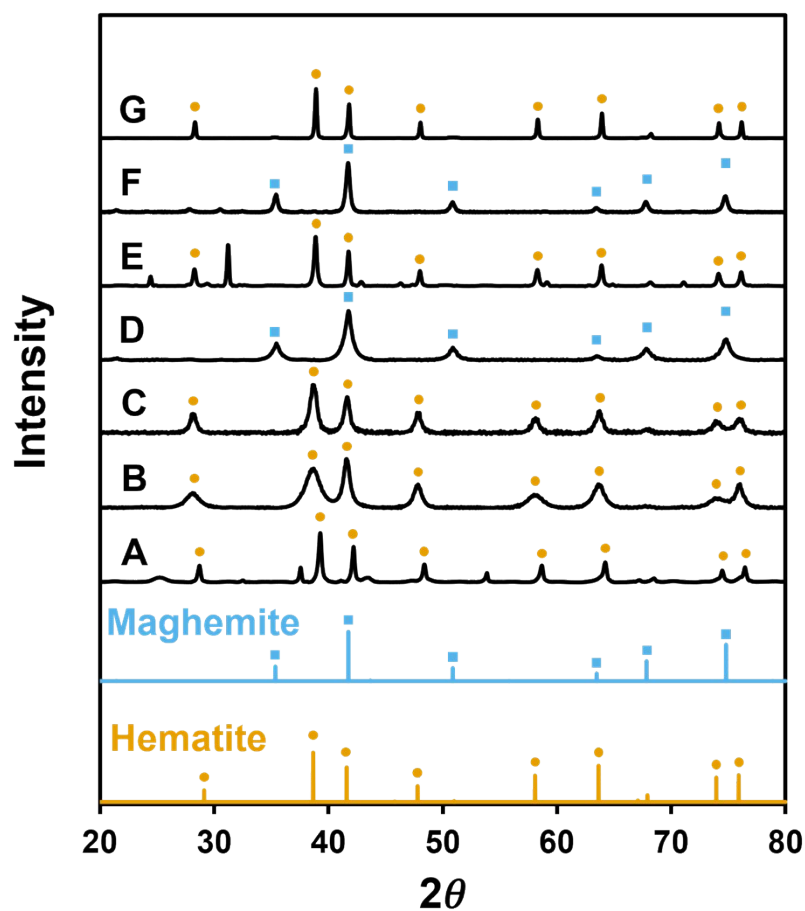
Fig. S4. X-ray Diffraction (XRD) patterns for Fe oxide particles from seven different commercial vendors. Also provided are reference XRD patterns for hematite (98-000-0060; JADE Software) and maghemite (98-000-1056; JADE Software), with key diffraction lines in each sample aligned to these reference patterns as indicated.
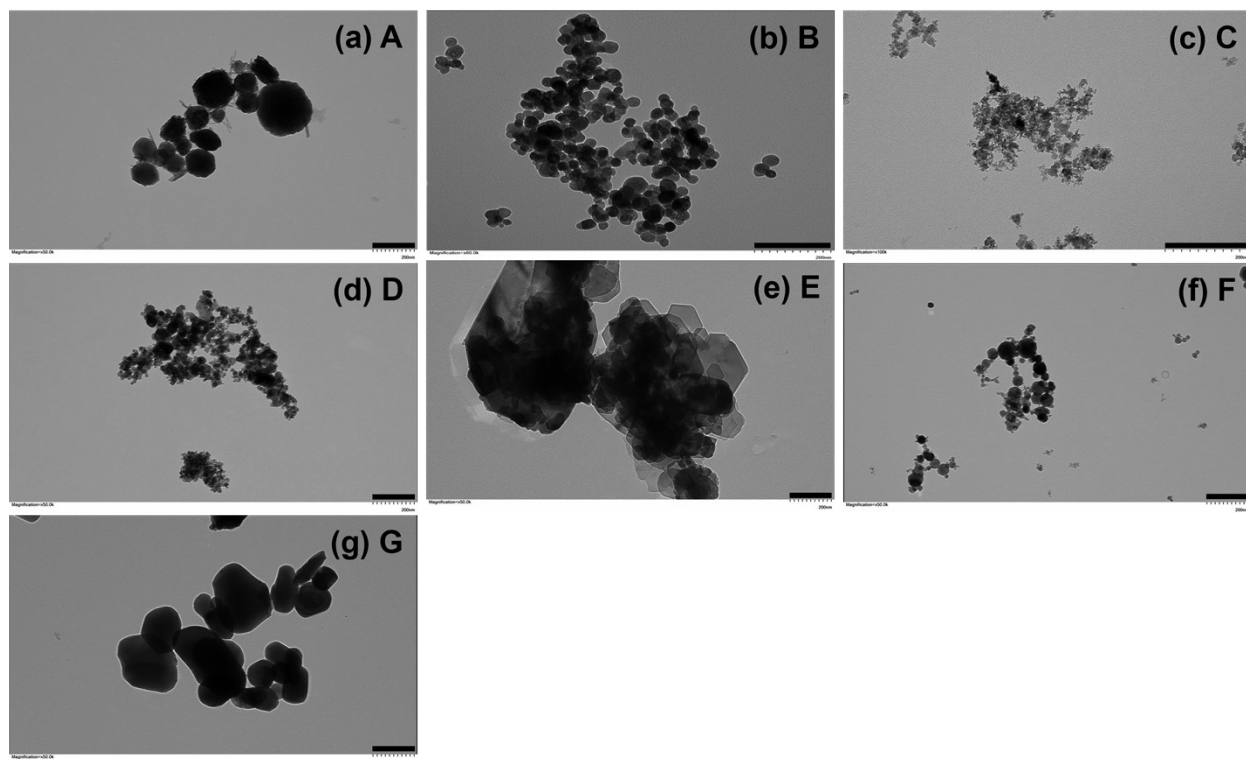
Fig. S5. TEM images for commercial Fe oxide particles from vendors A through G. For each image, the scale bar corresponds to 200 nm. Generally, particle sizes matched expectations of particle sizes and size ranges provided by the vendors.
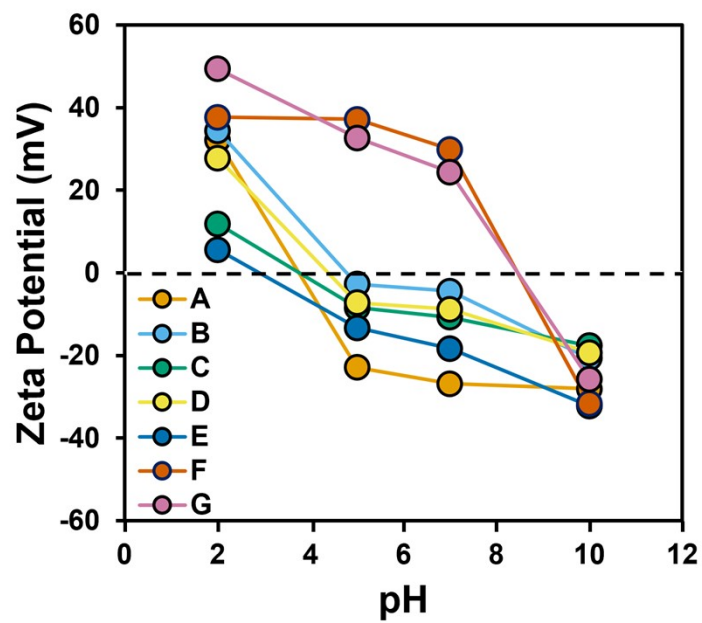
Fig. S6. Zeta potential for Fe oxide particles from seven different commercial vendors dispersed in DI water as a function of pH. Data are shown for suspensions prepared at pH 2, 5, 7, and 10.
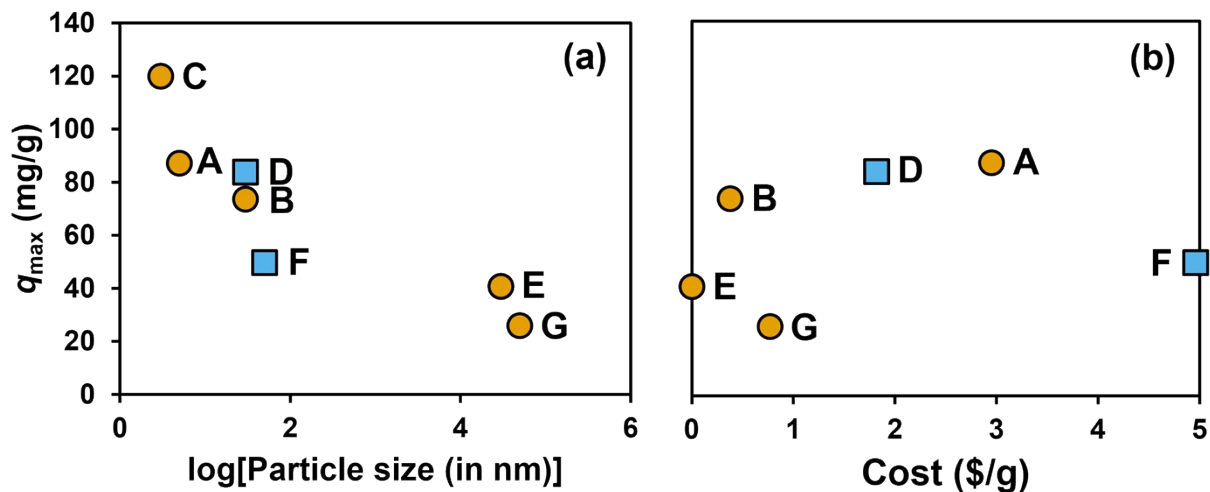
Fig. S7. Pb uptake capacity (q_{max} values from Langmuir isotherm model fits) for seven commercial Fe oxide particles shown as a function of (a) particle size (on a logarithmic scale) and (b) cost (USD per gram). Circles indicate those materials that XRD suggest are primarily hematite (i.e., Vendors A, B, C, E and G) and squares indicate those materials that XRD suggest are primarily maghemite (i.e., Vendors D and F). Because the Fe oxide from Vendor C has been discontinued and pricing information is no longer available, results for Vendor C were omitted from the data in panel (b).
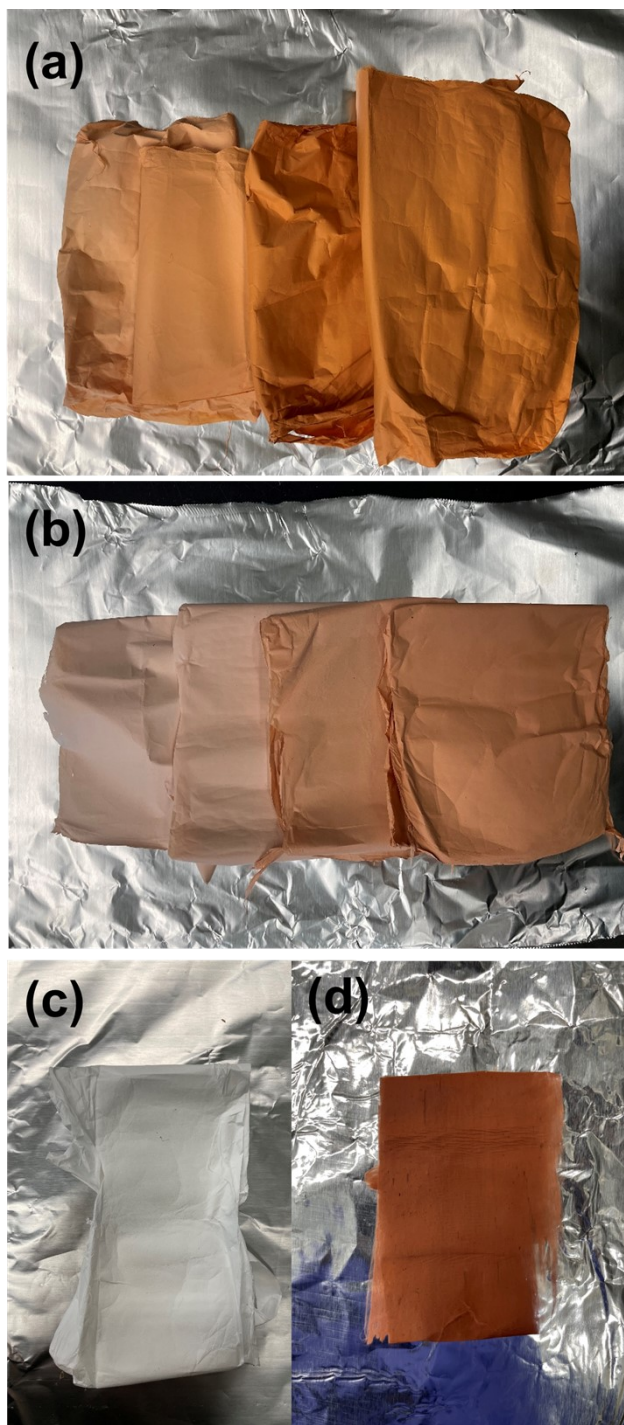
Fig. S8. Pictures of Fe-PAN composites illustrating the effect of increasing iron oxide loading (1 wt.%, 2 wt.%, 3 wt.%, and 5 wt.% relative to total mass) for composites prepared with Fe oxides from different vendors. Shown are pictures of Fe-PAN using oxides from (a) Vendor B and (b) Vendor D. For comparison, panel (c) shows a picture of pure PAN nanofibers, and panel (d) is a picture of one formulation, Fe5-PTA3, from Vendor E.
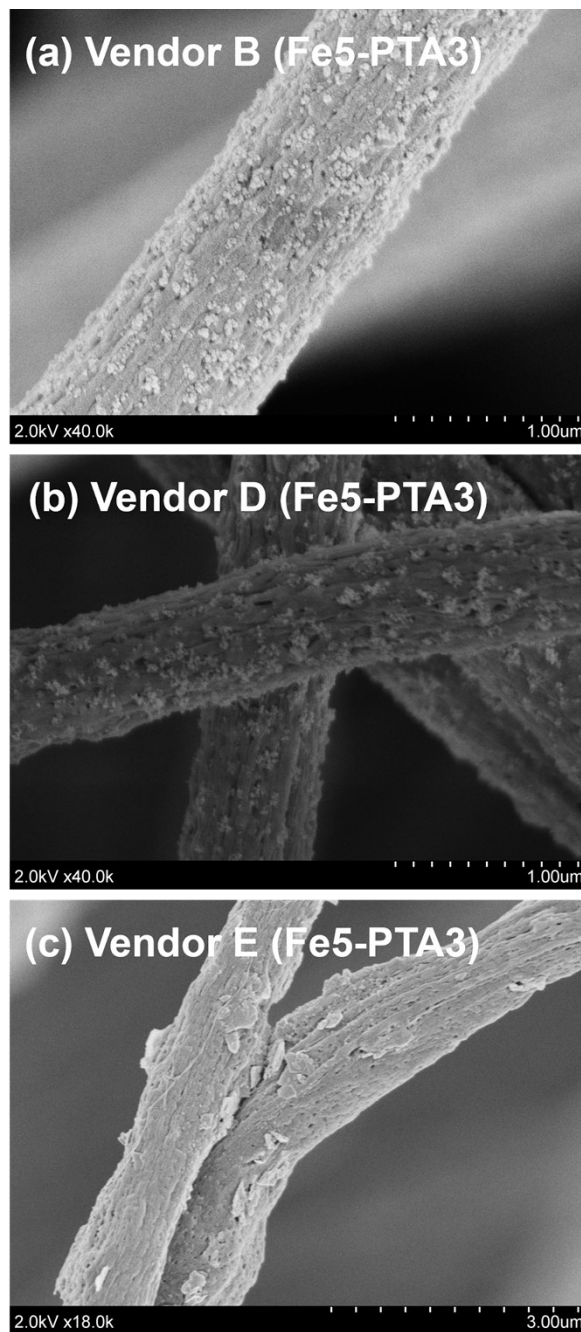
Fig. S9. SEM images for Fe5-PTA3 prepared using Fe oxides from Vendor (a) B, (b) D, and (c) E.
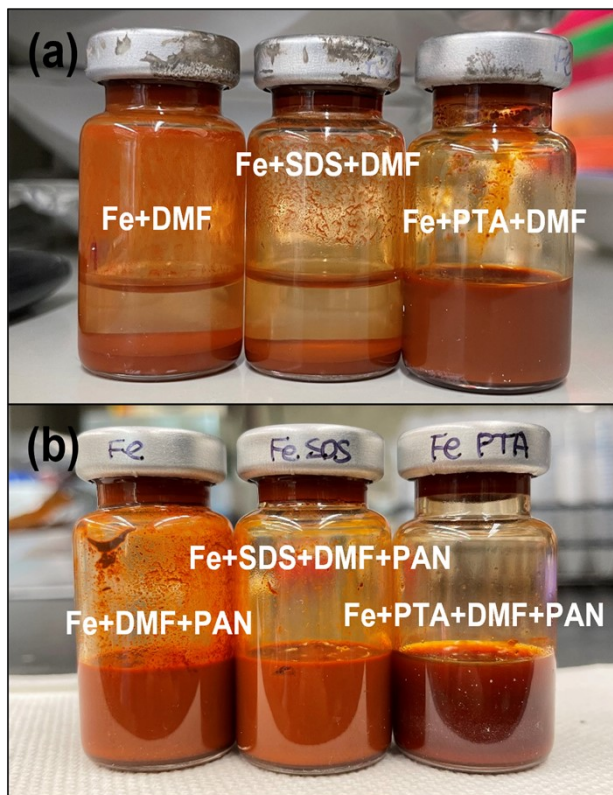
Fig. S10. Electrospinning sol gel precursor (a) before and (b) after adding the polymer (PAN) to the Fe oxide (Vendor B) and solvent (DMF) suspensions. Sol gel solutions containing organic additives SDS (with PAN) and PTA (both with and without PAN) were visibly more stable (i.e., not prone to settling), with uniform sol gel consistency, supporting the role of additives in promoting particle dispersion and suspension stability (i.e., limiting particle aggregation).
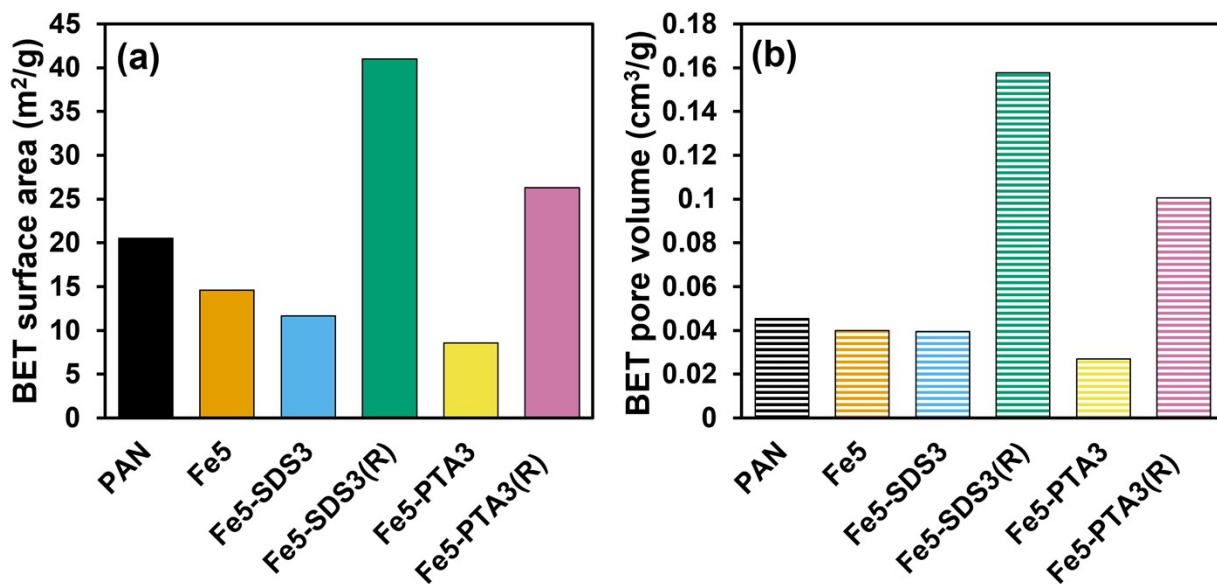
Fig. S11. (a) BET surface area and (b) pore volume for various nanofiber formulations, with composites prepared using Fe oxide particles from Vendor B. Whereas the addition of Fe oxide particles and organic additives generally decreased surface area and pore volume, presumably from the blocking of pores within PAN, rinsing of the composites releases the organic additives and results in large increases in both specific area and pore volume. Both SDS and PTA function as porogens, therefore, in addition to their ability to improve Fe oxide dispersion in the sol gel precursor and resulting electrospun nanofibers.
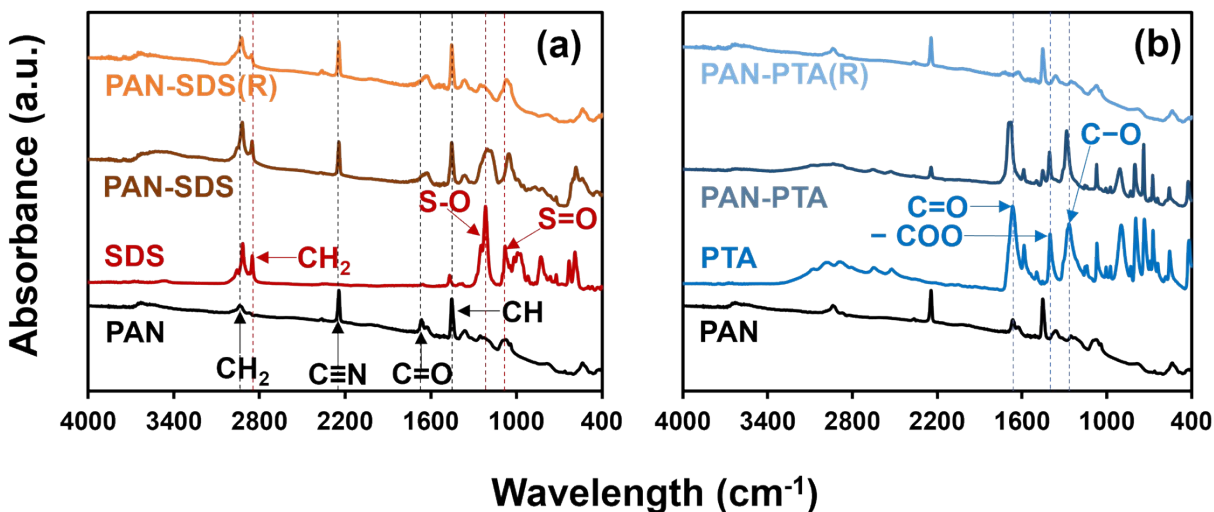
Fig. S12. FTIR spectra of (a) SDS- and (b) PTA-containing nanofiber composites, along with spectra obtained for pure PAN and powders of reagent grade SDS and PTA. For composites, spectra are shown both for as synthesized materials and after rinsing [denoted by (R)]. Spectral features previously assigned in the literature for functionalities in PAN, SDS, and PTA are noted. After rinsing, FTIR spectra revealed little signal attributable to inclusion of SDS and PTA, suggesting any amount of these organic additives retained in the fibers after rinsing must be below the level of detection by FTIR. As noted, the peaks at 2920 cm^{-1}, 2240 cm^{-1}, 1730 cm^{-1}, and 1450 cm^{-1} are associated with the presence of the CH$_2$, C≡N, C=O, and CH from PAN.[S3-S5] 2848 cm^{-1}, 1215 cm^{-1}, and 1083 cm^{-1} peaks are corresponding to CH$_2$, S−O, and S=O.[S6,S7] 1664 cm^{-1}, 1404 cm^{-1}, and 1265 cm^{-1} peaks are corresponding to C=O, COO, and C−O. [S8,S9]
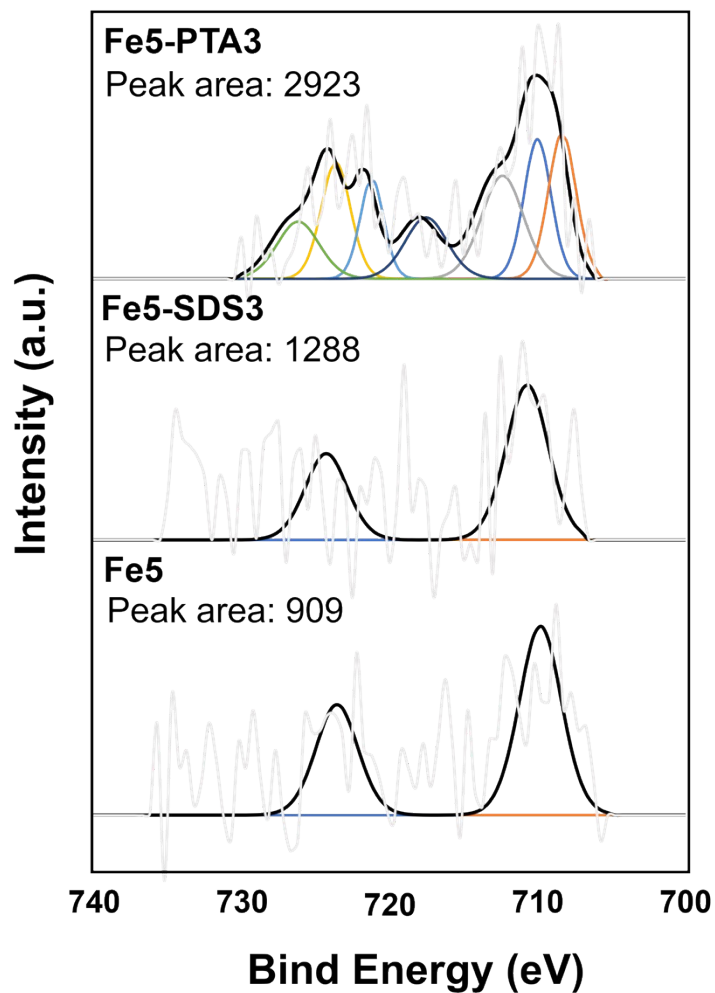
Fig. S13. High-resolution Fe2p XPS spectra for Fe5, Fe5-SDS3, and Fe5-PTA3 nanofiber composites (prepared using Fe oxide from Vendor B). Dark, solid black lines and underlying-colored areas indicate model fits to the spectra features associated with the embedded Fe oxide. Peak areas obtained from these model fits are shown, with an increase in surface Fe concentration for nanofiber composites prepared with PTA and SDS as organic additives.
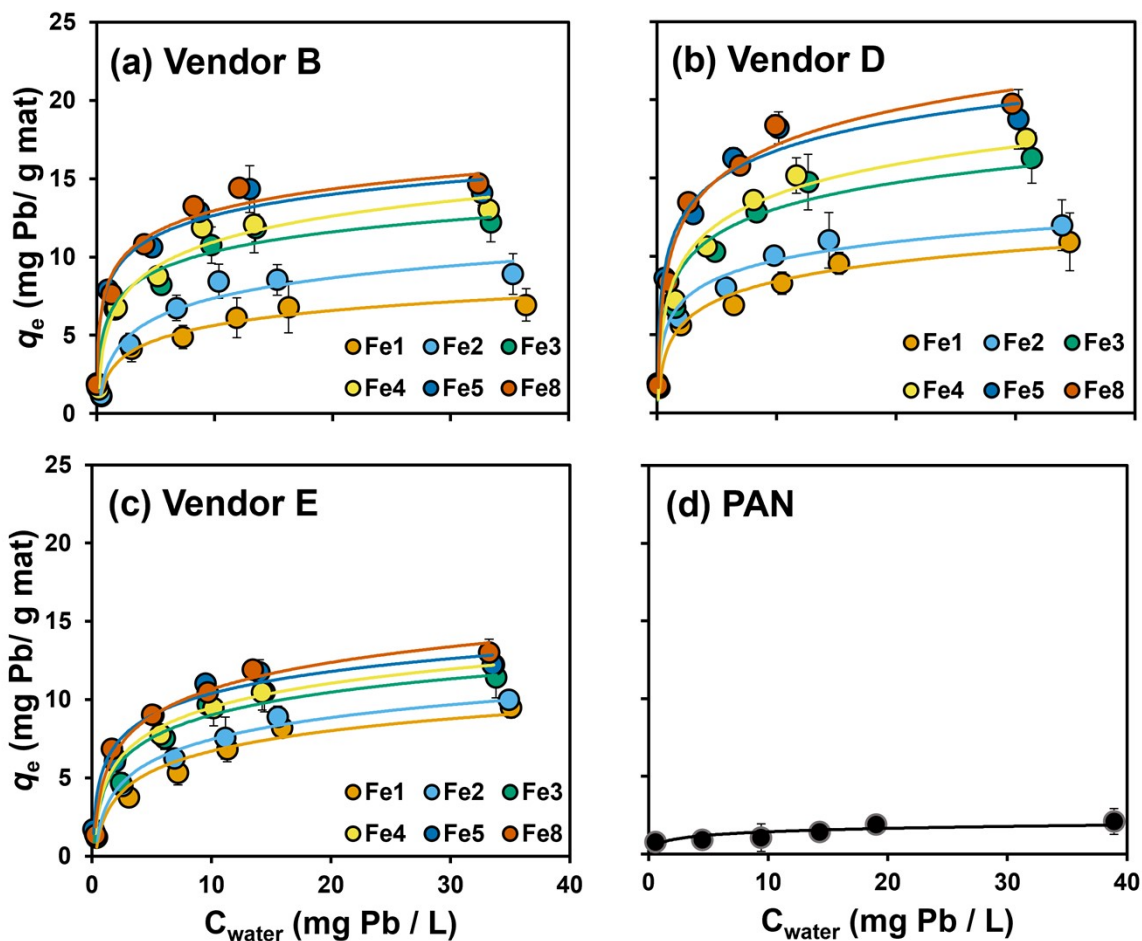
Fig. S14. Uptake isotherms for Pb by Fe-PAN nanofiber composites with different Fe loading (from 1 to 8 wt.%) and prepared using Fe oxides from Vendors (a) B, (b) D, and (c) E. For comparison, Pb sorption on unmodified PAN nanofibers (no Fe oxide) are shown in (d). Solid lines represent Langmuir isotherm model fits determined through non-linear regression analysis. Error bars represent one standard deviation from duplicated experiments. Experimental conditions: $C_{initial}$=1-40 mg/L as Pb; pH = 6.5 with 10 mM HEPES buffer; T = 20°C; dosage = 0.5 g/L; contact time = 24 h.
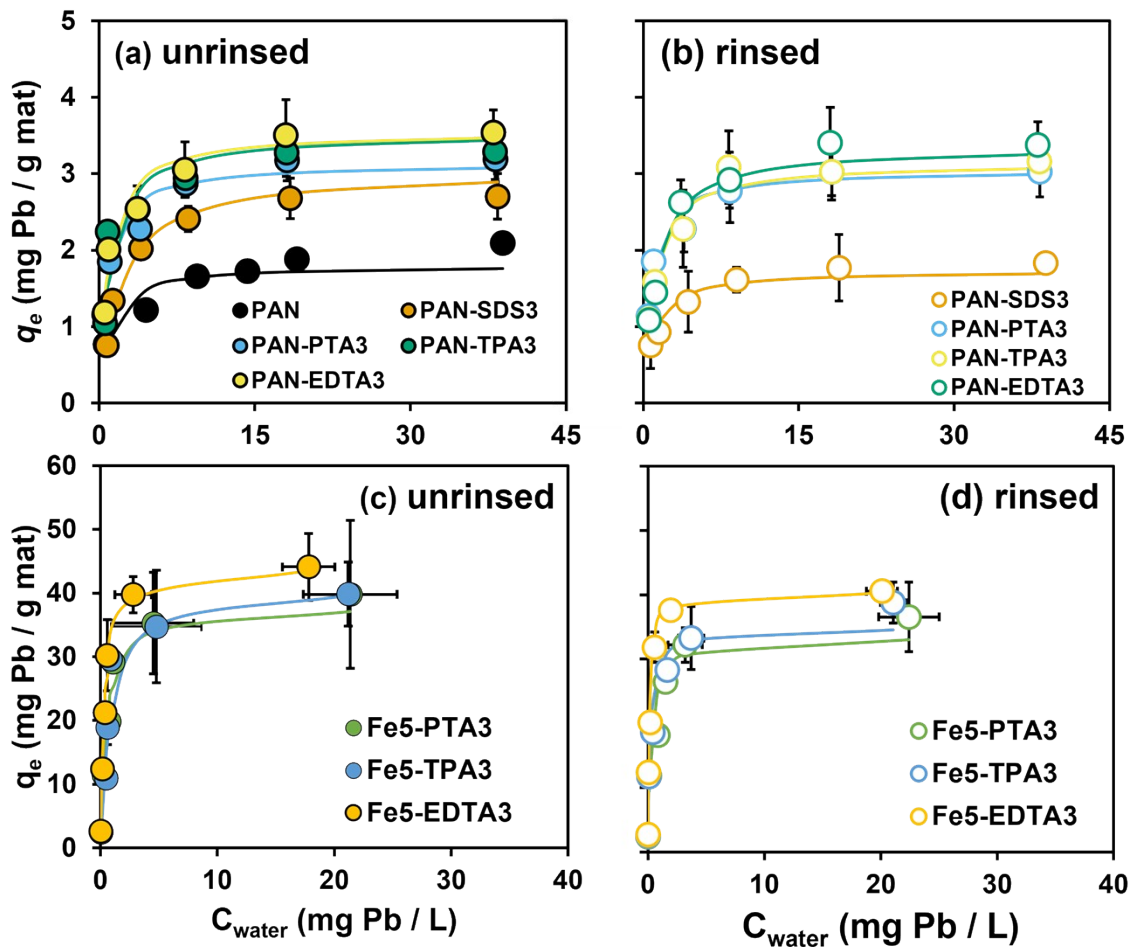
Fig. S15. Uptake isotherms for Pb by (a) unrinsed and (b) rinsed organic acid-functionalized PAN nanofibers (without Fe) and by (c) unrinsed and (d) rinsed Fe(B)-PAN functionalized with PTA and other carboxylic acids (TPA and EDTA). Solid lines represent Langmuir isotherm model fits determined through non-linear regression analysis. Error bars represent standard deviation from duplicate experimental trials. Experimental conditions: $C_{initial}$=1-40 mg/L as Pb; pH = 6.5 with 10 mM HEPES buffer; T = 20°C; dosage = 0.5 g/L; contact time = 24 h.
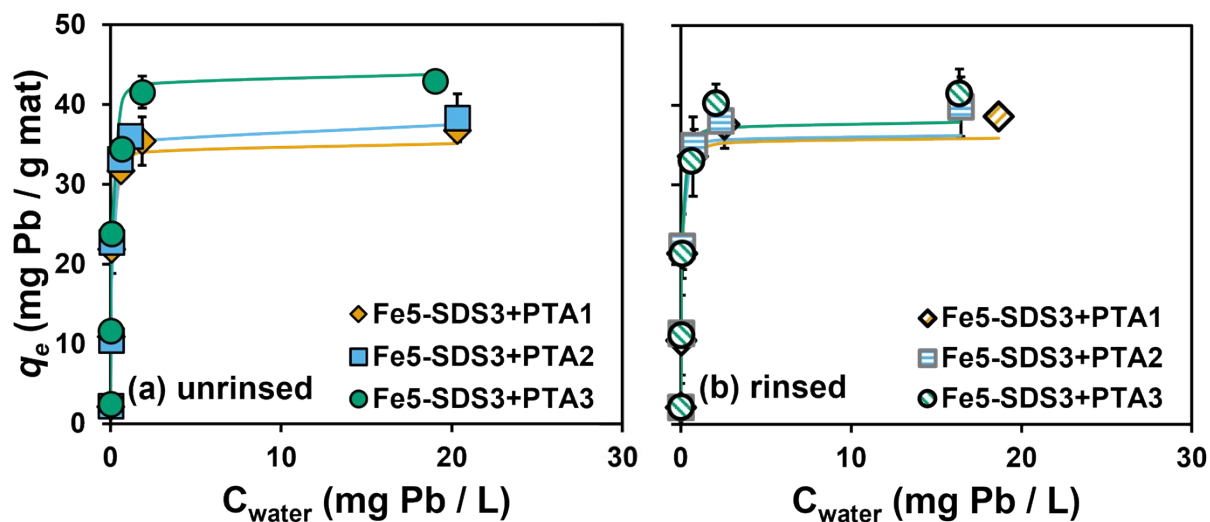
Fig. S16. Uptake isotherms for Pb by (a) unrinsed and (b) rinsed Fe5(B)-PAN functionalized with various combinations of SDS and PTA. Solid lines represent Langmuir isotherm model fits determined through non-linear regression analysis. Error bars represent standard deviation from replicate experimental trials. Experimental conditions: $C_{initial}$=1-40 mg/L as Pb; pH = 6.5 with 10 mM HEPES buffer; T = 20°C; dosage = 0.5 g/L; contact time = 24 h
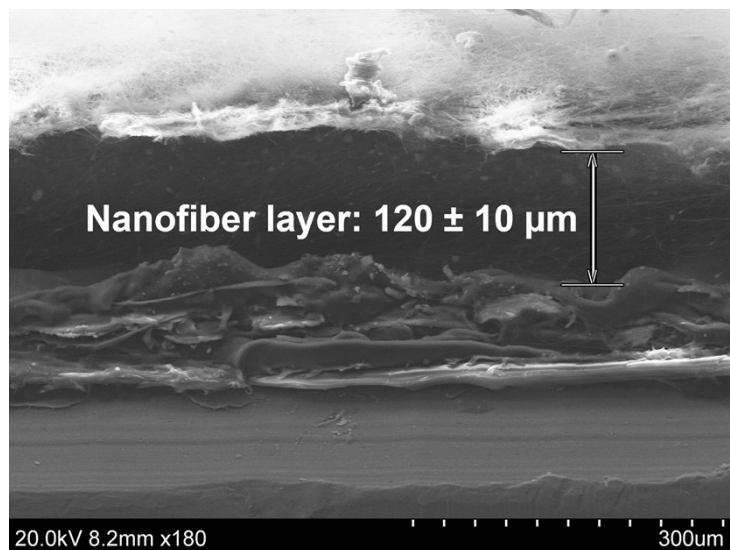
Fig. S17. Cross-sectional SEM image of Fe5(B)-PTA3, with measured nanofiber filter thickness shown. The thickness and its standard deviation were calculated from measurement of $n \geq 30$ cross sections within the same material using Image J software. These values were assumed representative for filter layers used in dead-end filtration experiments.

29
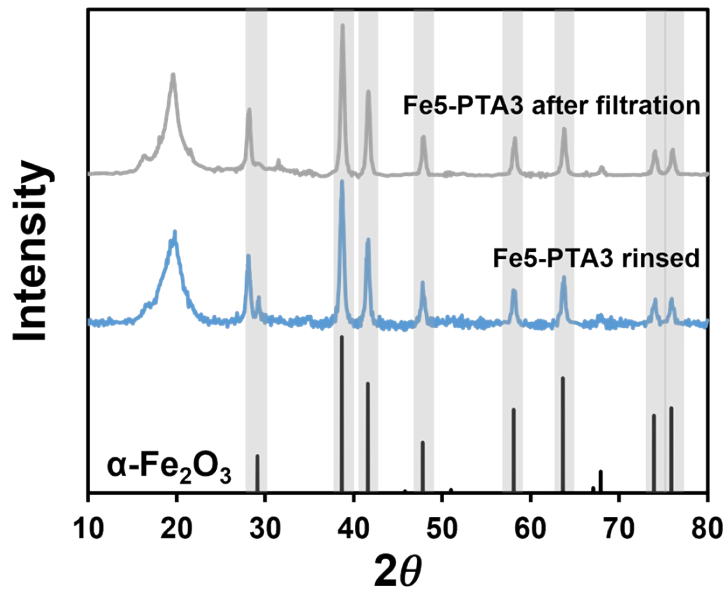
Fig. S18. XRD pattern of pristine Fe5(B)-PTA3 (blue) and Fe5(B)-PTA3 after dead end filtration trial with dissolved Pb (grey). The filtration conditions were 20 mL/min of flow rate, 150 µg Pb/L of initial feed, 4 L of total treated volume, and 4 layers of Fe5-PTA3.
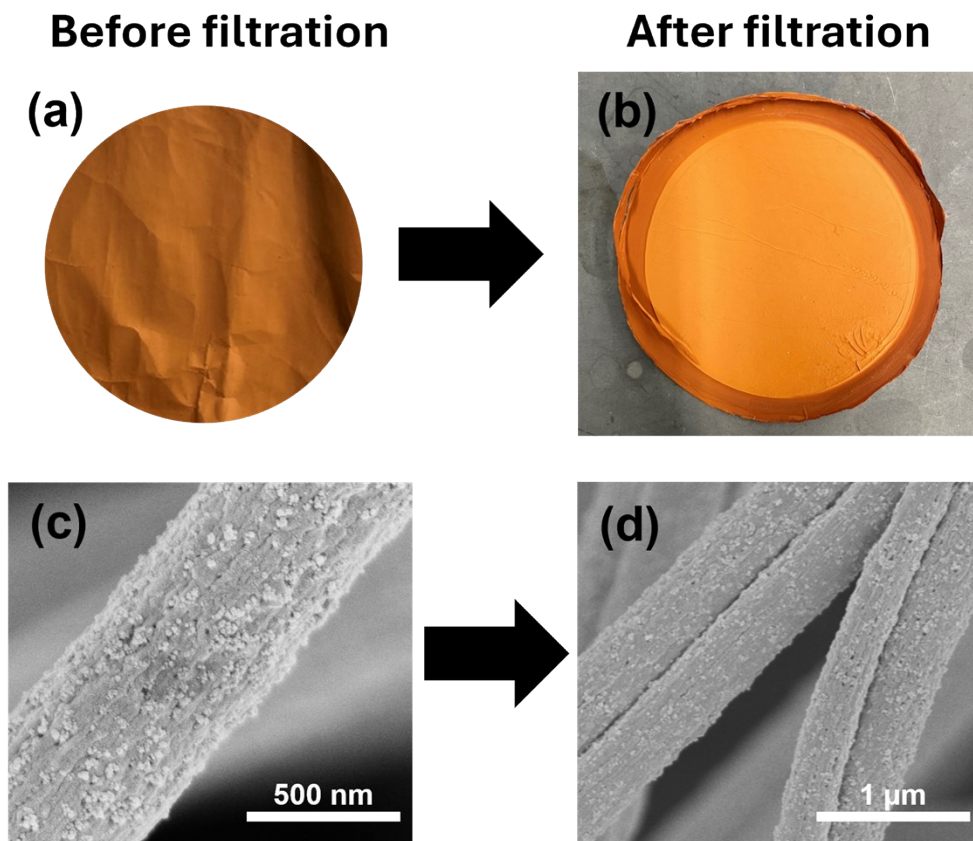
Figure S19. Digital images of Fe5-PTA3 composites (a) before and (b) after Pb filtration, with corresponding SEM images (c) before and (d) after Pb filtration, illustrating the retention of the embedded iron oxide particles and no obvious evidence of the formation of a lead-containing precipitate.
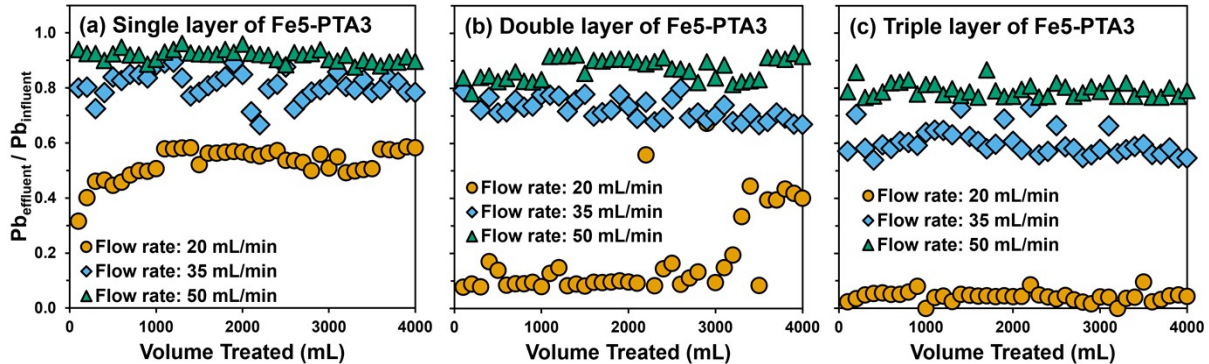
Fig. S20. Normalized dissolved lead concentration ($Pb_{effluent}/Pb_{influent}$) as a function of water volume passed through the filter for a (a) single layer, (b) double layer, and (c) triple layer of Fe5(B)-PTA3 in a dead-end filtration system (one layer of the mat is ~60 mg and ~120 μm in thickness). Data are shown for three volumetric flow rates: 20, 35 and 50 mL/min. Experimental conditions: Total feed volume = 4 L, $Pb_{influent}$ =150 μg/L, effective nanofiber area=12.6 cm^2, and pH 6.5 with 10 mM HEPES buffer.

Literature Cited

S1. Y.P. Kumar, P. King, and V. Prasad, Equilibrium and kinetic studies for the biosorption system of copper (II) ion from aqueous solution using Tectona grandis Lf leaves powder, *Journal of Hazardous Materials*, 2006. **137(2)**, 1211-1217.

S2. B. Chen, W. Sun, C. Wang, and X. Guo, Size-dependent impact of inorganic nanoparticles on sulfamethoxazole adsorption by carbon nanotubes, *Chemical Engineering Journal*, 2017, **316,** 160-170.

S3. I. Karbownik, M. Fiedot, O. Rac, P. Suchorska-Wozniak, T. Rybicki, and H. Teterycz, Effect of doping polyacrylonitrile fibers on their structural and mechanical properties, *Polymer*, 2015, **75**, 97-108.

S4. A. Jenab, R. Roghanian, N. Ghorbani, K. Ghaedi, and G. Emtiazi, The efficacy of electropsun PAN/Kefiran nanofiber and kefir in mammalian cell culture: promotion of PC12 cell growth, anti-MCF7 breast cancer cells activities, and cytokine production of PBMC, *International Journal of Nanomedicine*, 2020, **15**, 717-728.

S5. S. Tas, O. Kaynan, E. Ozden-Yenigun, and K. Nijmeijer, Polyacrylonitirle (PAN)/crown ether composite nanofibers for the selective adsorption of cations, *RSC Advances*, 2016, **6**, 3608-3616.

S6. A. Allahbakhsh and S. Mazinani, Influences of sodium dodecyl sulfate on vulcanization kinetics and mechanical performance of EPDM/graphene oxide nanocomposites, *RSC Advances*, 2015, **5**, 46694-46704.

S7. M. K. Singh, A. Agarwal, R. Gopal, R. K. Swarnkar, and R. J. Kotnala, Dumbbell shaped nickel nanocrystals synthesized by a laser induced fragmentation method, *Journal of Materials Chemistry*, 2011, **21**, 11074-11079.

S8. J. S. Loring, M. Karlsson, W. R. Fawcett, and W. H. Casey, Infrared spectra of phthalic acid, the hydrogen phthalate ion, and the phthalate ion in aqueous solution, *Spectrochimica Acta Part A: Molecular and Biomolecular Spectroscopy,* 2001, **57**, 1635-1642.

S9. Y. S. Hwang, J. Liu, J. J. Lenhart, and C. M. Hadad, Surface complexes of phthalic acid at the hematite/water interface, *Journal of Colloid and Interface Science*, 2007, **307**, 124-134.